Three-Dimensional Morphology Control during Wet Chemical Synthesis of Porous Chromium Oxide Spheres

Lifang Chen,[†] Zhi Song,[‡] Xue Wang,[†] Sergey V. Prikhodko,[§] Juncheng Hu,*[,‡] Suneel Kodambaka,[§] and Ryan Richards*[,†]

Department of Chemistry and Geochemistry, Colorado School of Mines, Golden, Colorado 80401, and Key Laboratory of Catalysis and Materials Science of Hubei Province, South-Central University for Nationalities, Wuhan 430074, China, and Department of Materials Science and Engineering, University of California Los Angeles, Los Angeles, California 90095

ABSTRACT Controlling the morphological evolution in nanostructures is essential for improving their functionality, for example, in catalysis. Here, we demonstrate, using chromium oxide as a model system, that morphologies of functional binary oxide particles can be tailored by an efficient template-free synthetic approach. We construct a morphological "phase diagram" for chromium oxide spheres that shows the evolution of size and surface roughness as a function of the precursor and urea concentrations. It is notable that these chromium oxide spheres show an exceptional ability to remove azo−dye pollutant in water treatment. Thus, the porous chromium oxide spheres with very good dye absorptions are expected to be useful in alternative absorption technologies.

KEYWORDS: binary oxides • chromium oxide • spheres • porous • pollutant

INTRODUCTION

Three-dimensional (3D) metal oxide micro- and nanostructures have received much attention because of their potential use in a wide range of applications in the fields of catalysis, separations, microelectronic devices, and biomaterial engineering (1−5). The self-assembly of inorganic nanostructured building blocks into 3D ordered hierarchical nanostructures is fascinating because variation of the arrangements of the building blocks provides a method to tune the properties of the material (6−8). In recent years, several methods including thermal reduction, thermal oxidation, oriented aggregation, the self-assembly of building blocks through hydrophobic interactions, and template-assisted synthesis, have been used to prepare complex 3D metal oxide nanostructures (9−12). In particular, the design and fabrication of spherical materials with hollow interiors or porosities have attracted considerable attention because of their potential uses in the release of drugs, dyes, and as catalysts (3, 9, 13−15). A variety of hollow micro/nanospheres have been fabricated based on template-assisted processes, followed by removal of the template materials by calcination or solvent extraction (9, 16). However, it remains a major challenge for scientists to develop simple, template-free, and reliable synthetic methods for hierarchically self-assembled architectures with designed chemical compositions and controlled morphologies that strongly affect the properties of nanomaterials.

The controlled synthesis and characterization of porous inorganic materials is a major objective in such technologies as catalysis, sorption, filtration, as well as thermal and acoustic insulation (16−18). Such materials include zeolites, mesoporous materials, as well as dried gel structures such as aerogels. Among them, zeolites and mesoporous materials have ordered pore structures, while aerogels have disordered pore structures. Recent efforts have largely emphasized surfactant templates on ordered structures; however, template-assisted processes have shortcomings for practical applications owing to the high cost, time requirement, and environmental concerns. Aerogels are highly porous architectures, but they generally lack homogeneous sizes and shapes. Recently, many researchers have made sustained efforts to prepare porous metal oxides with controlled shape, size, and dimensionality (12, 16, 17, 19−21). Various porous metal oxide morphologies, such as nanosheets, nanoplates, and hollow nanostructures, have been produced through various routes including hydrothermal synthesis, microwave-assisted precipitation, and ultrasonic spray pyrolysis. For instance, we have previously reported preparations of porous MgO and NiO nanosheets by a hydrothermal method (17, 19). Further, porous SiO_2−TiO_2 microspheres have been synthesized by ultrasonic spray pyrolysis, and porous ZnO nanoplates were generated by microwave-assisted precipitation (12, 21).

Increasingly stringent environmental standards increase the pressure to focus on air, water, and soil pollution as well as excessive natural resource consumption. Considerable attention has been paid to the environmental problems

* Corresponding authors. E-mail: rrichard@mines.edu (R.R.), junchenghuhu@hotmail.com (J.H.).
Received for review May 15, 2009 and accepted August 14, 2009
[†] Colorado School of Mines.
[‡] South-Central University for Nationalities.
[§] University of California Los Angeles.
DOI: 10.1021/am900334q

involving water treatment, especially with regard to organic refractory pollutants. It was estimated that 10−20% of the world azo−dye production was lost during the dyeing process and released into the environment by the textile industry (22). The release of toxic and hazardous dyes from these industries has created a global concern because of their immense toxicity toward mankind. A considerable amount of work has also been reported in the literature regarding the absorption of some dyes on various adsorbent surfaces such as activated carbon (23), silica (24), clay (25), natural polymers (26), synthetic polymer (27), and so on. Of the above-mentioned methods, there are some drawbacks including high temperature (or high energy requirement), high pressure, production of secondary pollution, the need for highly specialized biodegradable compounds, etc. Thus, it is necessary to pursue more "ideal" alternatives to activated carbon that would possess high absorption capacity, would be relatively easily and inexpensively produced, and would be readily recyclable. Because nanostructured metal oxides possess high surface area and low production costs and have a regenerative capacity through combustion of the adsorbed species, they represent a family of materials worthy of intensive investigations for absorption applications. In recent years, metal oxides such as MnO_2 and Fe_2O_3 nanostructures have been found to have high capacities to remove pollutants from wastewater because of their novel 3D hierarchical and porous structures (11, 28−33).

Herein, we report, for the first time, a template-free and halide-free efficient hydrothermal method to synthesize porous chromium oxide spheres using chromium nitrate as the starting material, and the preparation process leads to an excellent yield of 95% and high crystallinity of the products. Moreover, the porous chromium oxides have uniform size and surface morphologies that can be controlled by the preparation method. Moreover, the porous chromium oxide spheres exhibit very good dye absorptions, promising for applications in alternative absorption technologies.

EXPERIMENTAL SECTION

Preparation of Porous Chromium Oxide Nanospheres. All of the chemicals were received from Aldrich Corp., Madison, WI, and used without further purification. In a typical procedure, chromium nitrate [$Cr(NO_3)_3 \cdot 9H_2O$] was dissolved in methanol, and the solution was transferred to an autoclave with 7500 Torr argon pressure and kept at ca. 180 °C for 5 h and then at 265 °C (the pseudo-supercritical point of the solvent system). After supercritical fluid drying (via release of the pressure in the autoclave), a green powder was collected, subsequently calcined in air with a ramp rate of 3 °C/min to 500 °C, and then maintained at 500 °C for 4 h. The same procedures apply to different sizes and surface roughnesses of nanospheres, and the reaction conditions are given in the figure captions. A conventionally prepared chromium oxide powder (CP-Cr_2O_3) was obtained from decomposition of chromium nitrate at 500 °C for 4 h.

Absorption of Dye Pollutants. A total of 0.1 g of chromium oxide was added to 40 mL of a dye pollutant solution with a concentration of 100 mg/L under stirring at a rate of 150 rpm at room temperature. At the end of the absorption period, the solution was centrifuged for 10 min at 7000 rpm, after which small amounts of the liquid were analyzed by UV−vis absorption spectra. The spectra were monitored for changes in absorbance at a wavelength of maximum absorbance after being diluted five times. For comparison, the same experiments are performed on CP-Cr_2O_3.

Instrumentation. The materials were characterized by powder X-ray diffraction (XRD) using a Siemens D5000 X-ray diffractometer with nickel-filtered Cu Kα radiation ($\lambda = 1.5418$ Å) at a scanning rate of 0.1°/min in the 2θ range of 30−70°. A Thermo 6700 Fourier transform infrared (FTIR) spectrometer with a liquid-nitrogen-cooled mercury−cadmium−telluride detector, a high-temperature environmental chamber, and a diffuse-reflectance infrared Fourier transform spectroscopy (DRIFTS) accessory were used with the following parameters: 64 scans, 650−4000 cm^{-1} scan range, and 4 cm^{-1} resolution.

Nitrogen absorption−desorption isotherms were obtained using a Micrometrics ASAP 2020. The samples were degassed at 300 °C in a vacuum for more than 4 h prior to the measurement. The specific surface areas were evaluated with the Brunauer−Emmett−Teller (BET) method in the P/P_0 range of 0.05−0.35. Pore size distributions were calculated from the desorption branch of the isotherms with the Barrett−Joyner−Halenda method.

Field-emission scanning electron microscopy (FESEM) characterization of the samples was carried on a JEOL JSM-7000F. Dual-beam focused ion beam and scanning electron microscopy (FIB-SEM) was performed on a FEI Nova Nano 600. Transmission electron microscopy (TEM) imaging and electron diffraction characterization of the samples were carried out on JEOL JEM-100CX and JEM-2010 operated at 100 and 200 kV, respectively. A high-resolution TEM (HRTEM) study was performed on a FEI Titan operated at 300 kV. The samples for TEM were prepared by spreading of an ultrasonicated suspension in ethanol onto a grid as well as by dry deposition of the particles directly onto a grid.

RESULTS AND DISCUSSION

The uniform porous chromium oxide spheres were successfully prepared by a wet chemical technique. Defined chromium nitrate was dissolved in methanol, and the solution was transferred to an autoclave with 7500 Torr argon pressure, kept at ca. 180 °C for 5 h, and then at 265 °C for 5 h. After supercritical fluid drying, a green powder (as-synthesized chromium oxide precursor) was collected, subsequently calcined in air at 500 °C for 4 h, and referred to as porous chromium oxide spheres. Unless otherwise indicated, the same calcination procedure applies to all porous chromium oxide spheres. The morphology of the as-prepared chromium oxide was studied by FESEM, and the crystallinity was determined by XRD and the microstructure using TEM. Parts a and b−d of Figure 1 show the SEM images of the product before and after calcination, respectively, which imply that calcination did not change the spherical morphology of the sample. Figure 1a shows the precursor of chromium oxide, composed of spherical nanostructures with a smooth surface and a diameter of 1 μm. Owing to the alcoholysis and hydrolysis reactions of chromium nitrate, amorphous chromium alkoxide and chromium hydroxide formed from a methanol solution under hydrothermal conditions and quickly congregate to spherical aggregates in order to decrease their surface energies (35, 36). These spherical nanoparticles were dried under supercritical conditions in order to avoid their collapse. After calcination, the spherical morphology was maintained; however, the

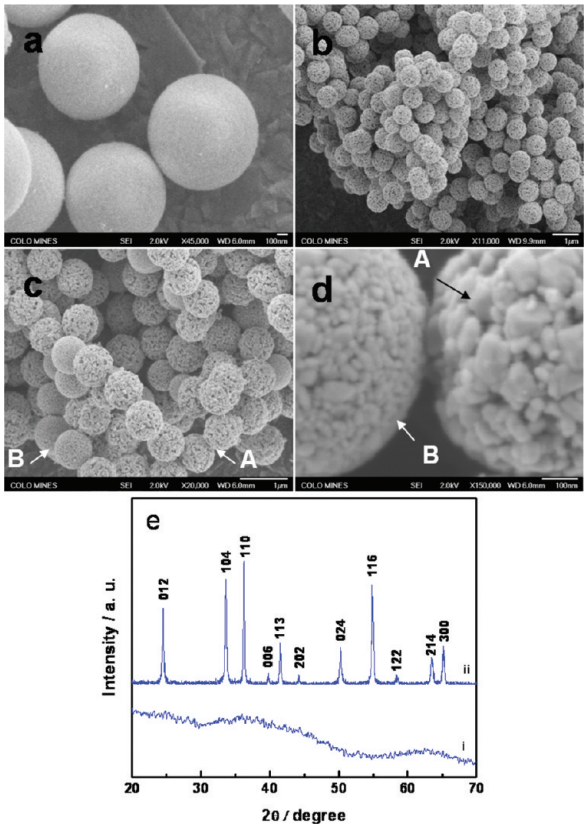

FIGURE 1. (a) FESEM image of the as-prepared chromium oxide precursor. (b−d) FESEM images of porous chromium oxide spheres (as-prepared chromium oxide precursor calcined in air at 500 °C for 4 h) at different magnifications. (e) Powder XRD patterns of (i) as-synthesized chromium oxide precursor and (ii) porous chromium oxide spheres. The sample was synthesized from a 0.025 M chromium nitrate solution.

diameter of these porous chromium oxide spheres decreased from 1 μm to ca. 800 nm, and nanometer-sized porous architectures were formed in the spheres because of the removal of organic species in the precursor by pyrolysis, which is shown in Figure 1b−d. Figure 1b shows that the sample is composed of many uniform porous spheres that are approximately 750 nm in diameter. The detailed morphologies of these spheres are shown in Figure 1c,d, which reveal that the entire structure is comprised of large amounts of nanoparticulates with a rough surface. These nanoparticulates are ca. 10−100 nm and aggregated together to form 3D porous spheres. It is interesting to note that the aggregates that are formed have a very narrow size distribution. Moreover, these porous chromium oxide spheres with distinctive differences are shown as two types of spheres (A and B). A and B are similar in size but different in surface roughness because of the differences in the assembly of the chromium oxide precursor aggregates produced during the aggregation process. Figure 1e (curve i) is a powder XRD pattern of the as-synthesized product and shows it is amorphous. This is also confirmed by selected-area electron diffraction (SAED) in the Supporting Information (Figure S1). We suggest that this is due to the formation of a mixture of chromium alkoxides and chromium hydroxide in the reaction system, where alkyl groups are covalently bonded to the oxygen atoms of the chromium oxide precursor (38). After calcination at 500 °C, the XRD pattern of the dark-green powder (Figure 1e, curve ii) shows a well-crystallized phase that can be indexed to the corundum phase of Cr_2O_3, according to the Joint Committee on Powder Diffraction Standards (JCPDS) card number 38-1479, with lattice spacings of $a = 0.4959$ nm and $c = 1.3538$ nm. These values are in excellent agreement with those reported for bulk α-Cr_2O_3 (39). The material crystallizes in a trigonal-hexagonal rhombohedral crystal system, space group $R\bar{3}c$, and is isostructural with α-Al_2O_3 (corundum) and α-Fe_2O_3 (hematite). From DRIFTS spectra of the as-synthesized product, we observed organic species in these amorphous spheres (see Figure 2a). The bands at 1086, 1353, 1414, 1572, 2822, and 2930 cm^{-1} are indicative of the presence of methoxyl groups, while the band at 1670 cm^{-1} corresponds to the bending vibrations of hydroxyl groups. The DRIFTS results indicate that large amounts of alkyl and hydroxyl groups are covalently bonded to the surface of the Cr_2O_3 precursor. After calcination at 500 °C (Figure 2b), these alkyl groups have been completely removed, and the pores are formed; however, the spherical morphology is maintained.

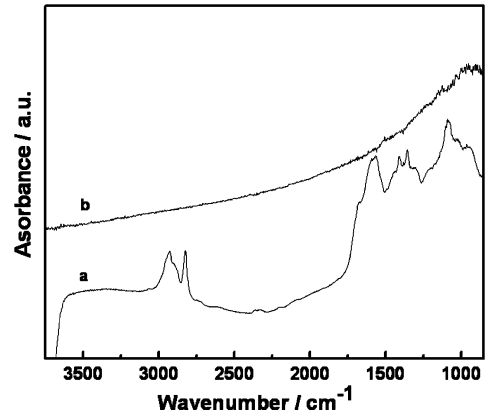

FIGURE 2. DRIFTS spectra obtained from an as-synthesized chromium oxide precursor (a) and porous chromium oxide spheres synthesized from a 0.025 M chromium nitrate solution (b).

Figure 3a shows a TEM image of a porous chromium oxide sphere with a diameter of ca. 800 nm. We note that these spheres are composed of smaller chromium oxide particles. From cross-sectional sectioning of these spheres, carried out using FIB milling, we determined that the cores are also composed of similar particles. It is interesting that these particles aggregate into 3D spheres, regardless of the rates of growth. Furthermore, the SAED analysis (Figure 3b) also confirmed that the particles are polycrystalline Cr_2O_3. From the SAED patterns, we measured interplanar spacings d_m. Table S1 in the Supporting Information contains the d_m values in comparison with JCPDS values (d_t) for the Cr_2O_3 corundum crystal structure and the corresponding planes. We find that the measured values are, within experimental error, in agreement with the JCPDS data as well as the XRD pattern of chromium oxide. A representative HRTEM image of the Cr_2O_3 nanoparticulate is shown in Figure 3c. The lattice fringes are clearly observed with a spacing of 0.359 nm, corresponding to the spacing of the (102) planes of Cr_2O_3 (the tabulated value is 0.362 nm). Fast Fourier transforms (FFTs) were taken from the area highlighted with the

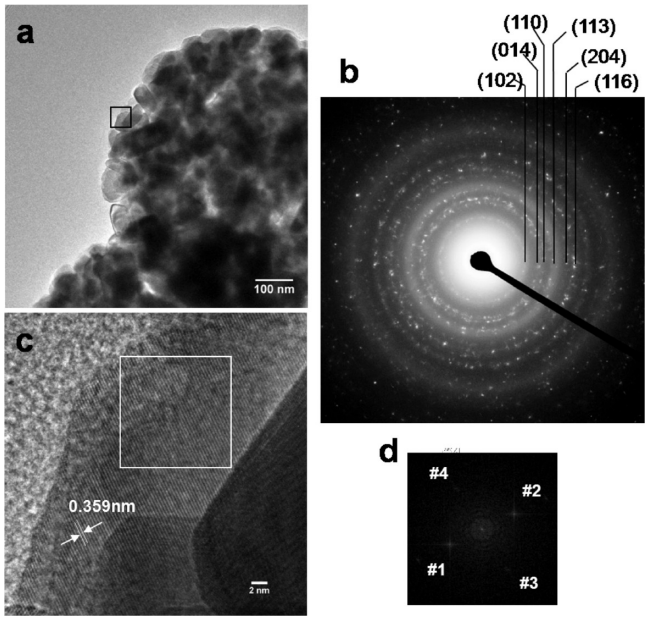

FIGURE 3. (a) TEM image of porous chromium oxide spheres synthesized from a 0.025 M chromium nitrate solution. (b) SAED pattern of an individual porous chromium oxide sphere. (c) HRTEM image of a selected region highlighted on image a. (d) FFT taken from the area highlighted with a white square on image c.

white square on Figure 3c. The four closest to the incident spots were measured, giving values 0.36, 0.37, 0.27, and 0.27 nm for the spots from 1 to 4, respectively. Spots 1 and 2 correspond to (102) reflections and spots 3 and 4 to (014) reflections of the $R\bar{3}c$ structure of Cr_2O_3 (tabulated values are 0.362 and 0.267 nm).

In order to investigate the inner structure of these porous chromium oxide spheres, FIB-SEM was used. Figure 4a demonstrates the two different types of spheres presented; it is shown as tilted (52°). The box shown with white color on the image is the area where a protective layer of platinum was deposited before cutting of the spheres using the ion beam. After the platinum layer was deposited (Figure 4b), a rectangular cross-sectional box was milled in front of the feature of interest (Figure 4c,d) with the ion beam of 30 kV and 3 nA. The cross-sectional area can be observed in the high-magnification SEM image (Figure 4e). It shows that the inner structure of the spheres is the same as their outer surface; these chromium oxide spheres are porous and composed of smaller nanoparticulates.

As shown in Figure 1, there are two different types of spheres (A and B) in our products. In order to understand the formation process of chromium oxide, we investigated the effect of urea and the precursor concentration on the morphology of chromium oxide spheres. Urea can change the hydrolysis and alcoholysis rates of chromium nitrate, while the precursor concentration is a measure of supersaturation in the solution. Figure 5 is a summary of the as-synthesized products obtained as a function of both the precursor (x axis) and urea (y axis) concentrations. In the absence of urea, a mixture of two kinds of porous chromium oxide spheres (A and B as shown in Figure 1b–d) has been obtained. However, in the presence of urea and with increasing amounts, the B-type spheres were obtained. Figure 5 along the y axis shows porous chromium oxide sphere morphologies obtained using urea concentrations of 0.06 and 0.18 M, respectively, at a constant precursor concentration of 0.025 M. When chromium nitrate reacts with methanol and water to form the chromium oxide precursor, acid is a byproduct, and the accumulation of acid will inhibit further formation of the chromium oxide precursor. When urea is added, the OH^- formed by urea hydrolysis neutralizes the acid and allows the fast formation of the chromium oxide precursor. Thus, in the self-assembly process, we suggest that the steady OH^- supply moderates the hydrolysis and alcoholysis rates of chromium nitrate via urea hydrolysis (see eqs 1–5) (11, 19, 38). High hydrolysis or alcoholysis rates lead to rapid aggregation of chromium oxide precursors in order to decrease their surface energies (35, 36). These aggregates form bigger spheres with smoother sur-

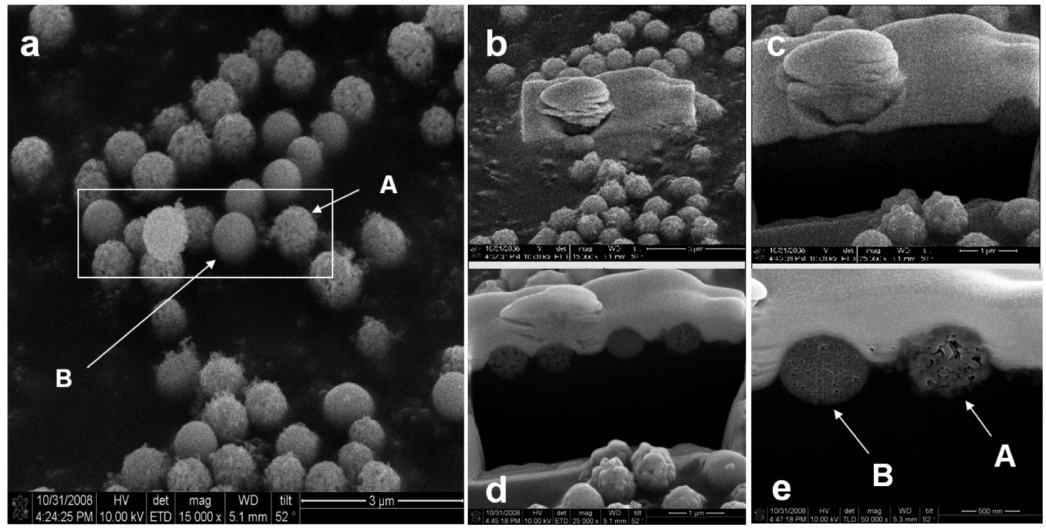

FIGURE 4. SEM images of (a) type A and B porous chromium oxide spheres (synthesized from a 0.025 M chromium nitrate solution) as tilted 52° before the deposition of a platinum protective layer, (b) after platinum layer deposition, (c) after milling of the rectangular cross-sectional box in front of the feature of interest, (d) the area of a cross-sectional cut polished with a fine ion beam, and (e) a high-magnification SEM image of the cross-sectional cut area.

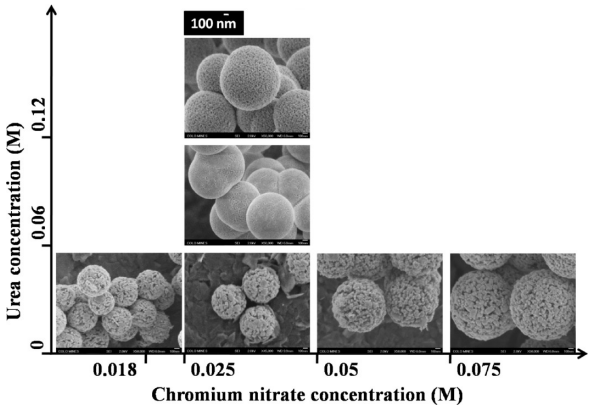

FIGURE 5. Morphological "phase diagram" of porous chromium oxide spheres shown as a function of the chromium nitrate concentration (*x* axis) and the urea concentration (*y* axis). All other parameters (time, temperature, etc.) are held constant. All of these images have the same magnification.

faces and smaller pores (Figure 5 along the *y* axis and Figure S2 in the Supporting Information) after calcination at 500 °C for 4 h. All of these spheres are examined using XRD, and the results show that these samples are the corundum crystal structure (Figure S3 in the Supporting Information). Therefore, the roughnesses of the chromium oxide spheres can be tuned by varying the amount of urea.

$$Cr(NO_3)_3 + 3CH_3OH \rightarrow Cr(OCH_3)_3 + 3HNO_3 \quad (1)$$

$$Cr(NO_3)_3 + 3H_2O \rightarrow Cr(OH)_3 + 3HNO_3 \quad (2)$$

$$CO(NH_2)_2 + H_2O \rightarrow CO_2 + 2NH_3 \quad (3)$$

$$NH_3 + H_2O \rightarrow NH_4^+ + OH^- \quad (4)$$

$$OH^- + HNO_3 \rightarrow H_2O + NO_3^- \quad (5)$$

The effect of the precursor concentration on the powder morphologies is also shown in Figure 5 along the *x* axis. As expected, smaller porous spheres with diameter of ca. 600 nm were obtained when the chromium nitrate concentration was 0.018 M. The size of porous chromium oxide spheres increased with increasing concentrations of chromium nitrate, as shown in Figure 5 along the *x* axis. For example, when the chromium nitrate concentration was 0.075 M, the size of the porous chromium oxide spheres was ca. 1.4 μm and was almost 2 times larger than that of porous spheres when the concentration was 0.025 M (Figure 5 along the *x* axis). If the chromium nitrate concentration was too low, the product could not form the spherical architecture, but the aggregates still appeared to be porous in structure (Figure 6). According to the experimental results, this indicates that these chromium oxide precursors are not sufficiently able to interconnect with other Cr_2O_3 precursors and aggregate together. Therefore, the sizes of the aggregates can then be

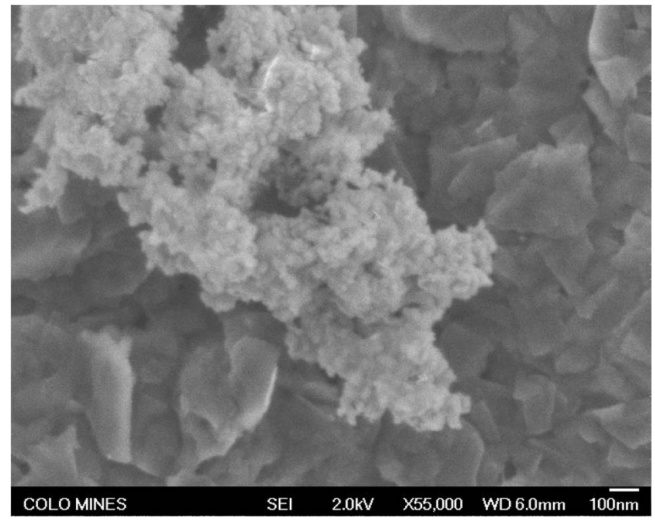

FIGURE 6. SEM image of chromium oxide calcined at 500 °C for 4 h. It was synthesized from a 0.008 M chromium nitrate solution.

tuned by varying the concentrations of chromium nitrate. With increased concentrations of chromium nitrate, these chromium oxide precursors will undergo continuous aggregation. However, the overall trend of the aggregation at different concentrations of chromium nitrate will be the same as that given here. These porous spheres under different concentrations of chromium nitrate are all similar to each other regarding the porous structure, surface roughness, and chromium oxide nanoparticulates. Thus, the sizes of the porous chromium oxide spheres strongly depend on the concentration of chromium nitrate.

In summary, increasing the urea concentration increases the chromium oxide nucleation rates, while increasing the precursor concentration leads to increased chromium oxide precursor aggregation in order to decrease their surface energies. An examination of the literature reveals there are no previous reports of porous chromium oxide spheres. Here, regular porous chromium oxide spheres have been synthesized (Figure 5), and it is further established that varying porosities and sizes of chromium oxide spheres are accessible and can be controlled by varying the concentrations of urea and chromium nitrate. Moreover, XRD results also show that all of these chromium oxide samples are corundum structures (Figures S3 and S4 in the Supporting Information).

In the quest for a sustainable future, considerable attention has been directed toward the environmental problems involving water treatment in recent years. Through the development of nanoscience and nanotechnology, it has been suggested that many of the current water-treatment problems could be resolved or greatly ameliorated by using nanosorbents, nanocatalysts, bioactive nanoparticles, catalytic membranes with nanostructures, etc. (11, 28−33). Many researchers have used metal oxide nanomaterials to remove toxic ions and organic pollutants from water, and these materials show higher removal capacities than bulk material (28−34). Because of the porous nature of the chromium oxide spheres from this work, their potential for application in dye pollutant removal from water was studied.

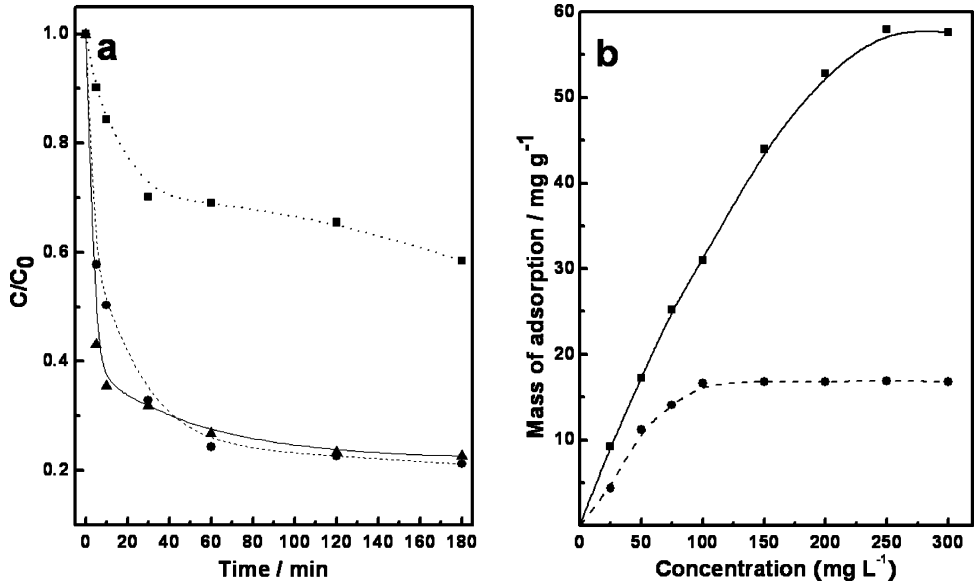

FIGURE 7. (a) Absorption rate of Congo red on new porous chromium oxide spheres (solid line), recovered porous chromium oxide spheres (dashed line), and CP-Cr_2O_3 (dotted line) with an initial concentration of 100 mg·g^{-1}. (b) Absorption isotherms of Congo red on chromium oxide spheres (solid line) and CP-Cr_2O_3 (dashed line). The new porous chromium oxide spheres were synthesized by a 0.025 M chromium nitrate solution.

Nitrogen absorption isotherms show that BET specific surface areas are 113 and 32 $m^2 \cdot g^{-1}$ for as-synthesized and calcined porous chromium oxide spheres (0 M urea and 0.025 M chromium nitrate), respectively. The decreased surface area is due to crystallization of the amorphous as-synthesized chromium oxide precursor. Table S2 in the Supporting Information shows the specific areas and pore structure parameters of chromium oxides with different concentrations of urea and chromium nitrate. The chromium oxides prepared in the absence of urea have similar specific surface areas that may be due to their similar porosities, regardless of the sizes of the spheres, while the surface area decreased with increasing urea concentration and constant chromium nitrate concentration because of smaller porosities. The high surface area and porosity are beneficial for absorption and various catalytic reactions. Because the chromium oxide nanospheres are large (~ micrometers), the solid/liquid separation would be fairly easy. In fact, porous chromium oxide spheres could be recovered efficiently by a simple catalytic combustion procedure to remove organic pollutants because of their stability at high temperatures.

Herein, we used the calcined porous chromium oxide spheres as adsorbents/catalysts to remove organic waste from water by absorption and subsequent catalytic combustion at relatively low temperatures (32). Congo red, a common azo−dye in the textile industry, was chosen as a typical organic dye waste. When the initial concentration of Congo red in solution was 100 mg·L^{-1}, the chromium oxide removed 75% of the Congo red at room temperature (20 °C), as shown by the solid line in Figure 7a, with a removal capacity of 30.0 (mg of Congo red)·g^{-1}. The electrostatic attraction between the surface and the Congo red species in solution and porosity absorption are responsible for the dye removal (23, 24, 26, 27). Furthermore, the chromium oxide containing Congo red is readily regenerated by catalytic combustion at 500 °C in air for 3 h, and the recovered chromium oxide powders maintained almost the same absorption performance as that shown by the dashed line in Figure 7a. Moreover, porous chromium oxide maintained its structure after regeneration, as shown in Figure S5 in the Supporting Information by the XRD pattern. For comparison, the same experiments are performed on CP-Cr_2O_3 (with a specific surface area of 11.5 $m^2 \cdot g^{-1}$), which is shown by the dotted line in Figure 7a, with a removal capacity of 16.6 (mg of Congo red)·g^{-1}. The absorption isotherms of Congo red by chromium oxide at different initial concentrations are illustrated in Figure 7b. They reveal that the mass of absorption increased with an increase of the initial concentration. The Langmuir absorption model is used to represent the relationship between the amount of dye adsorbed at equilibrium (q_e, mg·g^{-1}) and the equilibrium solute concentration (C_e, mg·L^{-1}): $q_e = q_m K C_e/(1 + KC_e)$ where q_m (mg·g^{-1}) is the maximum sorption capacity corresponding to complete monolayer coverage and K is the equilibrium constant (L·mg^{-1}) (40). The values of q_{max} and k are determined from the linear regression plot of C_e/q_e vs C_e. Model fits to equilibrium absorption results of Congo red were assessed based on the value of the determination coefficient (R^2) of the linear regression plot. The resulting plots are shown in Figure S6 in the Supporting Information. Table S3 in the Supporting Information summarizes the Langmuir absorption model constants and the determination coefficients. When such a model was adopted to analyze the absorption isotherms, the maximum absorption capacities (q_m) of the as-obtained chromium oxide for experiment and the Langmuir absorption model were found to be 57.6 and 64.2 (mg of Congo red)·g^{-1}, respectively. We also investigated the removal capacity of a CP-Cr_2O_3 powder under the same experimental conditions as those shown in Figure 7b (dashed line) and Table S3 in the Supporting Information. It is found that the removal capacities of this CP-Cr_2O_3 for experiment and the

Langmuir absorption model were 16.8 and 19.2 (mg of Congo red) $\cdot g^{-1}$. Obviously, the 3D chromium oxide spheres show much better removal capacity than those of CP-Cr_2O_3. The R^2 of the Langmuir model for CP-Cr_2O_3 (0.996 61) is better than that of chromium oxide spheres (0.983 17). The better absorption capacity for water treatment could be attributed to the porous structure and high specific surface area of chromium oxide.

CONCLUSION

In summary, we have synthesized chromium oxide with uniform, self-assembled, and porous spheres by an efficient wet chemical synthetic approach. The prepared chromium oxides have porous sphere morphologies composed of semiorganized aggregates of a large number of nanoparticle "building blocks". The sizes and surface roughnesses of chromium oxide spheres can be controlled by varying the concentration of precursor and the amount of urea. It is notable that chromium oxide spheres, with high surface area and porous structure, show an exceptional ability to remove azo−dye pollutant in water treatment. Thus, the porous chromium oxide spheres with very good dye adsorptions are expected to be useful in alternative absorption technologies.

Acknowledgment. Financial support from the Colorado School of Mines, the South-Central University for Nationalities (Grant YZZ 08002) and National Natural Science Foundation (Grant 20803096) of China, and the American Chemical Society Petroleum Research Foundation (Grant 48108-G10).

Supporting Information Available: SEM images, indexing of the SAED, surface area, pore parameters, Langmuir absorption isotherm parameters, and XRD. This material is available free of charge via the Internet at http://pubs.acs.org.

REFERENCES AND NOTES

(1) Mann, S. *Angew. Chem., Int. Ed.* **2000**, *39*, 3393–3406.
(2) Service, R. F. *Science* **2005**, *309*, 95–95.
(3) Mo, M.; Yu, J. C.; Zhang, L. Z.; Li, S. K. A. *Adv. Mater.* **2005**, *17*, 756–760.
(4) Gracias, D. H.; Tien, J.; Breen, T. L.; Hsu, C.; Whitesides, G. M. *Science* **2000**, *289*, 1170–1172.
(5) Cao, A. M.; Hu, J. S.; Liang, H. P.; Wan, L. J. *Ange. Chem., Int. Ed.* **2005**, *44*, 4391–4395.
(6) Niederberger, M.; Bard, M. H.; Stucky, G. D. *J. Am. Chem. Soc.* **2002**, *124*, 13642–13643.
(7) Niederberger, M.; Pinna, N.; Polleux, J.; Antonietti, M. *Angew. Chem., Int. Ed.* **2004**, *43*, 2270–2273.
(8) Niederberger, M.; Garnweitner, G.; Pinna, N.; Antonietti, M. *J. Am. Chem. Soc.* **2004**, *126*, 9120–9126.
(9) Lou, X. W.; Archer, L. A.; Yang, Z. C. *Adv. Mater.* **2008**, *20*, 3987–4019.
(10) Sinha, A. K.; Suzuki, K. *Angew. Chem., Int. Ed.* **2005**, *44*, 271–273.
(11) Zhong, L. S.; Hu, J. S.; Liang, H. P.; Cao, A. M.; Song, W. G.; Wan, L. J. *Adv. Mater.* **2006**, *18*, 2426–2431.
(12) Suh, W. H.; Jang, A. R.; Suh, Y. H.; Suslick, K. S. *Adv. Mater.* **2006**, *18*, 1832–1837.
(13) Mohanan, J. L.; Arachchige, I. U.; Brock, S. L. *Science* **2005**, *307*, 397–400.
(14) Viswanath, B.; Kundu, P.; Mukherjee, B.; Ravishankar, N. *Nanotechnology* **2008**, *19*, 1–7.
(15) Viswanath, B.; Ravishankar, N. *Biomaterials* **2008**, *29*, 4855–4863.
(16) Brock, S. L. *Science* **2007**, *317*, 460–461.
(17) Zhu, K. K.; Hu, J. C.; Kubel, C.; Richards, R. *Angew. Chem., Int. Ed.* **2006**, *45*, 7277–7281.
(18) Hu, J. C.; Zhu, K.; Chen, L. F.; Kubel, C.; Richards, R. *J. Phys. Chem. C* **2007**, *111*, 12038–12044.
(19) Hu, J. C.; Zhu, K. K.; Chen, L. F.; Yang, H. J.; Li, Z.; Suchopar, A.; Richards, R. *Adv. Mater.* **2008**, *20*, 267–271.
(20) Lou, X. W.; Wang, Y.; Yuan, C. L.; Lee, J. Y.; Archer, L. A. *Adv. Mater.* **2006**, *18*, 2325–2329.
(21) Jing, Z.; Zhan, J. *Adv. Mater.* **2008**, *20*, 4547–4551.
(22) Zollinger, H. *Synthesis, Properties and Applications of Organic Dyes and Pigments*; VCH: New York, 1987.
(23) Valix, M.; Cheung, W. H.; McKay, G. *Langmuir* **2006**, *22*, 4574–4582.
(24) Yan, Z.; Li, G. T.; Mu, L.; Tao, S. Y. *J. Mater. Chem.* **2006**, *16*, 1717–1725.
(25) Ozdemir, Y.; Dogan, M.; Alkan, M. *Microporous Mesoporous Mater.* **2006**, *96*, 419–427.
(26) Lazaridis, N. K.; Kyzas, G. Z.; Vassiliou, A. A.; Bikiaris, D. N. *Langmuir* **2007**, *23*, 7634–7643.
(27) Bekiari, V.; Lianos, P. *Chem. Mater.* **2006**, *18*, 4142–4146.
(28) Fei, J. B.; Cui, Y.; Yan, X. H.; Qi, W.; Yang, Y.; Wang, K. W.; He, Q.; Li, J. B. *Adv. Mater.* **2008**, *20*, 452–456.
(29) Zhong, L. S.; Hu, J. S.; Cao, A. M.; Liu, Q.; Song, W. G.; Wan, L. J. *Chem. Mater.* **2007**, *19*, 1648–1655.
(30) Wu, R. C.; Qu, J. H.; Chen, Y. S. *Water Res.* **2005**, *39*, 630–638.
(31) Herrera, F.; Lopez, A.; Mascolo, G.; Albers, E.; Kiwi, J. *Appl. Catal. B* **2001**, *29*, 147–162.
(32) Wu, R. C.; Qu, H. H.; He, H.; Yu, Y. B. *Appl. Catal. B* **2004**, *48*, 49–56.
(33) Yu, C. C.; Dong, X. P.; Guo, L. M.; Li, J. T.; Qin, F.; Zhang, L. X.; Shi, J. L.; Yan, D. S. *J. Phys. Chem. C* **2008**, *112*, 13378–13382.
(34) Song, Z.; Hu, J.; Chen, L.; Richards, R. *Nanotechnology* **2009**, *20*, 275707. (9pp).
(35) Viswanath, B.; Patra, S.; Munichandraiah, N.; Ravishankar, N. *Langmuir* **2009**, *25*, 3115–3121.
(36) Li, J.; Zeng, H. C. *J. Am. Chem. Soc.* **2007**, *129*, 15839–15847.
(37) Chen, L. F.; Hu, J. C.; Richards, R. M. *ChemPhysChem* **2008**, *9*, 1069–1078.
(38) Vayssieres, L.; Manthiram, A. *J. Phys. Chem. B* **2003**, *107*, 2623–2625.
(39) Park, J.; Kang, E.; Son, S. U.; Park, H. M.; Lee, M. K.; Kim, J.; Kim, K. W.; Noh, H. J.; Park, J. H.; Bae, C. J.; Park, J. G.; Hyeon, T. *Adv. Mater.* **2005**, *17*, 429–434.
(40) Langmuir, I. *J. Am. Chem. Soc.* **1918**, *40*, 1361–1403.

AM900334Q